

# Tectonics

## RESEARCH ARTICLE

10.1029/2018TC005364

### Key Points:

- Local earthquake tomography and hypocenter relocation was performed using seismicity across Haiti from 2013–2014
- Continued seismic activity was observed along Haiti's Southern Peninsula, associated with faults that ruptured during the Mw 7.0 2010 earthquake
- Hypocenters and a low velocity zone observed beneath the Massif de la Selle suggest a major south dipping thrust structure

### Supporting Information:

- Supporting Information S1
- Data Set S1

### Correspondence to:

D. Possee,  
djp1g15@soton.ac.uk

### Citation:

Possee, D., Keir, D., Harmon, N., Rychert, C., Rolandone, F., Leroy, S., et al. (2019). The tectonics and active faulting of Haiti from seismicity and tomography. *Tectonics*, 38, 1138–1155. <https://doi.org/10.1029/2018TC005364>

Received 9 OCT 2018










Accepted 22 FEB 2019

Accepted article online 5 MAR 2019

Published online 29 MAR 2019

©2019. American Geophysical Union.  
All Rights Reserved.

## The Tectonics and Active Faulting of Haiti from Seismicity and Tomography

Daniel Possee<sup>1</sup> , Derek Keir<sup>1,2</sup> , Nicholas Harmon<sup>1</sup> , Catherine Rychert<sup>1</sup> , Frédérique Rolandone<sup>3</sup> , Sylvie Leroy<sup>3</sup> , Jordane Corbeau<sup>3,4</sup> , Graham Stuart<sup>5</sup>, Eric Calais<sup>6</sup> , Finnigan Illsley-Kemp<sup>1,7</sup> , Dominique Boisson<sup>8</sup>, Roberte Momplaisir<sup>8</sup>, and Claude Prépetit<sup>9</sup>

<sup>1</sup>Ocean and Earth Science, National Oceanography Centre, University of Southampton, Southampton, UK, <sup>2</sup>Dipartimento di Scienze della Terra, Università degli Studi di Firenze, Florence, Italy, <sup>3</sup>Sorbonne Université, CNRS-INSU, Institut des Sciences de la Terre Paris (iSTeP), Paris, France, <sup>4</sup>IPGP, Observatoire de la Martinique, Paris, France, <sup>5</sup>School of Earth and Environment, University of Leeds, Leeds, UK, <sup>6</sup>Ecole normale supérieure, Department of Geosciences, Université PSL, Paris, France, <sup>7</sup>School of Geography, Environment and Earth Sciences, Victoria University of Wellington, Wellington, New Zealand, <sup>8</sup>Faculté des Sciences, Université d'Etat d'Haiti, Port-au-Prince, Haiti, <sup>9</sup>L'Unité Technique de Sismologie (UTS)/BME, Port-au-Prince, Haiti

**Abstract** Oblique convergence of the Caribbean and North American plates has partitioned strain across a major transpressional fault system that bisects the island of Hispaniola. The devastating  $M_w$  7.0, 2010 earthquake that struck southern Haiti, rupturing an unknown fault, highlighted our limited understanding of regional fault segmentation and its link to plate boundary deformation. Here we assess seismic activity and fault structures across Haiti using data from 33 broadband seismic stations deployed for 16 months. We use traveltimes tomography to obtain relocated hypocenters and models of  $V_p$  and  $V_p/V_s$  crustal structure. Earthquake locations reveal two clusters of seismic activity. The first corresponds to aftershocks of the 2010 earthquake and delineates faults associated with that rupture. The second cluster shows shallow activity north of Lake Enriquillo (Dominican Republic), interpreted to have occurred on a north-dipping thrust fault. Crustal seismic velocities show a narrow low-velocity region with an increased  $V_p/V_s$  ratio (1.80–1.85) dipping underneath the Massif de la Selle, which coincides with a southward-dipping zone of hypocenters to a depth of 20 km beneath southern Haiti. Our observations of seismicity and crustal structure in southern Haiti suggests a transition in the Enriquillo fault system from a near vertical strike-slip fault along the Southern Peninsula to a southward-dipping oblique-slip fault along the southern border of the Cul-de-Sac-Enriquillo basin. This result, consistent with recent geodetic results but at odds with the classical seismotectonic interpretation of the Enriquillo fault system, is an important constraint in our understanding of regional seismic hazard.

### 1. Introduction

The oblique convergence of the Caribbean and North American plates at 19 mm/year has resulted in a transpressive fault system that affects the island of Hispaniola (Haiti and Dominican Republic; Calais et al., 2016). Previous geophysical studies into crustal structure have mainly focused on the epicentral region of the  $M_w$  7.0, 12 January 2010 Haitian earthquake, revealing a network of subsurface faults which accommodates strain across the broader fault zone (Calais et al., 2010; Douilly et al., 2013; Wang et al., 2018). Regional crustal structure across Haiti has also been constrained by the use of receiver functions (Corbeau, Rolandone, et al., 2017).

The 2010 Haiti earthquake highlighted the importance of understanding crustal structures in seismic hazard assessment. Prior to the event, there was no knowledge of the Léogâne fault, the main fault which ruptured, with regional fault slip models only being able to incorporate a single vertical strike-slip fault, the Enriquillo-Plantain Garden Fault (EPGF, Figure 1; Manaker et al., 2008). Only through inversions of ground motion data recorded during the 2010 earthquake was the oblique rupture on the Léogâne fault recognized (Calais et al., 2010; Symithe et al., 2013) and later confirmed by precise aftershock relocations (Douilly et al., 2013). While the 2010 Haiti earthquake led to a vast improvement in our understanding of the regional seismotectonics, historical records indicate this is not the only region on the island capable of producing a devastating earthquake (Figure 1; Bakun et al., 2012; Prentice et al., 2010; ten Brink et al., 2011).

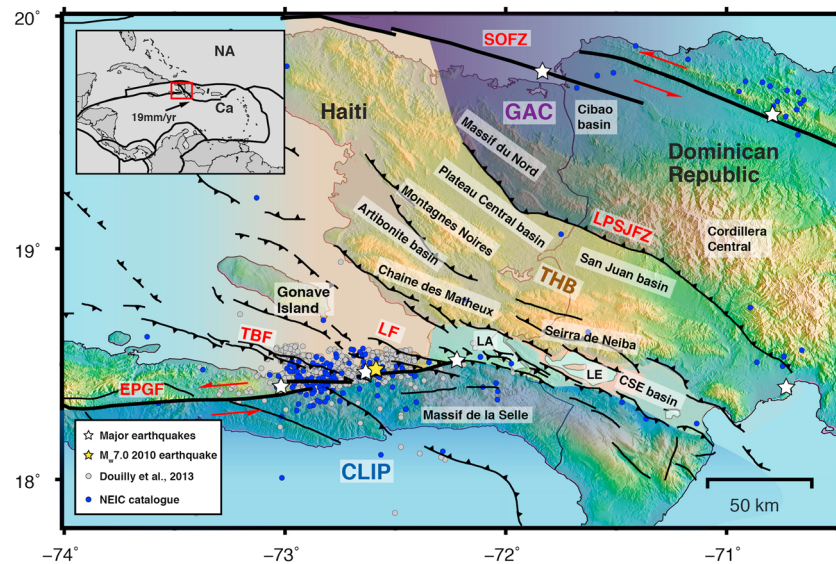


**Figure 1.** Tectonic map of Hispaniola (Haiti and Dominican Republic). Regional map in top left shows the relative motion of the Caribbean plate (Ca) and North American plate (NA). Circles show previous seismicity catalogs for Haiti: blue = Douilly et al. (2013); gray = National Earthquake Information Centre. Stars represent major historic earthquakes (Bakun et al., 2012; Prentice et al., 2010). Tectonic domains after Corbeau, Rolandone, et al. (2017): CLIP = Caribbean Large Igneous Province (blue); THB = Trans-Haiti deformation belt (brown); GAC = Greater Antilles Arc (purple). CSE = Cul-de-Sac-Enriquillo basin. Black lines show the surface trace of major faults: EPGF = Enriquillo-Plantain Garden fault zone; SOFZ = Septentrional-Oriente fault zone; LPSJFZ = Los Posos-San Juan fault zone; TBF = Trois Baies Fault system; LA = Lake Azuei, LE = Lake Enriquillo.

The aim of this paper is to use the Trans-Haiti seismic network to analyze local earthquakes, determining hypocenter locations, a local magnitude scale, and 2.5-D crustal models for  $P$  wave velocity ( $V_p$ ) and  $V_p/V_s$  ratios. The spatial coverage of the Trans-Haiti network, consisting of 27 temporary broadband seismometers, provides an excellent opportunity to assess both the distribution of seismicity 3 years after the 2010 Haitian earthquake and crustal structure at a regional scale across Haiti. This is crucial for understanding how the crust is modified by active tectonics and for future hazard assessment.

### 1.1. Tectonic Setting

Geological and geophysical studies have shown that Haiti is formed from three distinct tectonic domains (Figure 1). Northern Haiti is part of the Great Arc of the Caribbean, which initially formed by subduction along an inter-American transform fault at  $\sim 135$  Ma during the Cretaceous (Burke, 1988; Hastie et al., 2013; Pindell et al., 2012). During the eastward movement of the Caribbean plate, the Great Arc became inactive toward the end of the Upper Cretaceous, subsequently colliding with the Bahamas carbonate platform and fragmenting to form the Greater Antilles islands (Cuba, Jamaica, Hispaniola, Puerto Rico, and Virgin Islands; Cruz-Orosa et al., 2012; Hastie et al., 2013; Leroy et al., 2000; Mann et al., 1995). It has been estimated that the Great Arc constitutes two thirds of Hispaniola and consists of dominantly volcanic arc and forearc-accretionary prism facies (Mann et al., 1991).

The southern tectonic domain of Haiti is part of the Caribbean Large Igneous Province (CLIP), which consists of the Caribbean oceanic plateau and magmatic terranes along the Pacific coast of Central America and western Columbia, associated with the initiation of the Galapagos hotspot in the mid-Cretaceous (Duncan & Hargraves, 1984; Geldmacher et al., 2003; Pindell, 1990). The CLIP outcrops on the Southern Peninsula of Haiti and has been geophysically imaged south and west of Haiti (Calmus, 1983; Corbeau, Rolandone, Leroy, Mercier de Lépinay, et al., 2016; Leroy et al., 2000; Mauffret & Leroy, 1997; Mauffret et al., 2001). The presence of the CLIP is consistent with elevated  $V_p/V_s$  ratios of  $\sim 1.80$ , which are typical for mafic crustal rocks, seen in velocity models from local earthquake tomography (Douilly et al., 2016) and  $P$ -to- $S$  receiver functions (Corbeau, Rolandone, et al., 2017) along the Southern Peninsula of Haiti.

The central domain is a collisional wedge between the CLIP and Great Arc of the Caribbean, which began forming in the Early Miocene (Pubellier et al., 1991). As a result, it is characterized by a significantly thicker region of 40-km-thick crust, compared to 20–30 km thick for the northern and southern domains (Corbeau, Rolandone, et al., 2017). Geological studies have indicated the crust in this domain is of island arc origin, with either a back-arc or Cretaceous-Eocene remnant arc origin (Heubeck et al., 1991; Mann et al., 1991). *P*-to-*S* receiver function analysis found this thick central domain to have a mean  $V_p/V_s$  of 1.80 (Corbeau, Rolandone, et al., 2017). This was inconsistent with a purely island arc crust; therefore, Corbeau, Rolandone, et al. (2017) inferred the presence of dense material, which they interpreted to be related to either, Quaternary volcanics generated from a subcontinental lithospheric mantle (Kamenov et al., 2011) or mafic CLIP material from the south trapped in central Haiti early in its evolution.

## 1.2. Faulting

Haiti is bisected by two major left-lateral strike-slip faults, the Septentrional-Oriente fault zone (SOFZ) in the north, which has been mapped offshore (Calais & Mercier de Lépinay, 1995; Leroy et al., 2015; Rodríguez-Zurrunero et al., 2019), and the EPGF in the south (Figure 1; Mann et al., 1995). Between these faults, the fold and thrust belt, known as the Trans-Haiti belt and active in the Miocene and Pliocene, controls much of the relief on Haiti (Pubellier et al., 1991). It extends westward, forming the Gonâve Island as well as transpressive structures offshore (Corbeau, Rolandone, Leroy, Meyer, et al., 2016; Granja-Bruña et al., 2014), and eastward up to the Muertos Trough (Byrne et al., 1985; Ladd et al., 1977). South of Gonâve Island, there is a series of southward dipping faults extending 50 km, known as the Trois Baies thrust system (Mercier de Lépinay et al., 2011; Momplaisir, 1986; Wang et al., 2018).

Initial slip models for the  $M_w$  7.0, 2010 Haitian earthquake indicated the rupture initiated on a south dipping EPGF (Hashimoto et al., 2011; Hayes et al., 2010). However, recent consensus has switched to an oblique rupture on a north dipping structure, interpreted to be the Léogâne fault, that intersects the south-dipping EPGF at depth (Calais et al., 2010; Douilly et al., 2013). This hypothesis explained the lack of surface rupture, aftershock patterns, and shoreline uplift and was later supported by slip models of the rupture (Douilly et al., 2015; Hayes et al., 2010; Kocel et al., 2016; Saint Fleur et al., 2015; Symithe et al., 2013). Aftershocks clustered on both the EPGF, Léogâne fault and Trois Baies fault system (Douilly et al., 2013; Mercier de Lépinay et al., 2011), which was consistent with static slip models and Coulomb stress changes (Douilly et al., 2015; Saint Fleur et al., 2015). Focal mechanisms from aftershocks also indicated mostly reverse faulting on WNW-ESE-oriented faults dipping south at 30–40° (Nettles & Hjörleifsdóttir, 2010). The 2010 rupture therefore highlighted that the mode of faulting in southern Haiti is not simply a near vertical strike-slip fault system. Instead, there are many structures oblique to the main EPGF trace, which also have shallower dips and appear to me more seismically active.

The EPGF is well-expressed offshore west of Haiti and shows a clear trace in the surface morphology on Haiti's Southern Peninsula (Bourgueil et al., 1988; Cowgill et al., 2012; Prentice et al., 2010; Wessels et al., 2019). However, its surface expression is much less clear eastward of where the fault intersects the Cul-de-Sac-Enriquillo (CSE) basin (Figure 1, 72.3°W). Early geological work mapped the EPGF as terminating against reverse faults bounding the southern edge of the CSE basin (Bourgueil et al., 1988). Cowgill et al. (2012) more recently observed a left-lateral offset in the EPGF at a site to the east of Port-au-Prince, at the boarder of the CSE basin. In the CSE basin, Mann et al. (1995) and Wang et al. (2018) described curvilinear en echelon drag folds and interpreted them to mark the surface trace of the EPGF cross cutting the basin. East-west linear structures observed in chirp sonar profiles from Lake Azuei and Lake Enriquillo have also been used to interpret the presence of the EPGF crossing the CSE basin (Rios et al., 2013; Wang et al., 2018).

Saint Fleur et al. (2015) used air photographs and LIDAR topography to suggest that some of the folds in the CSE basin are fault propagation folds over shallow décollements, rooted on a major south-dipping reverse fault beneath the Massif de la Selle. GPS data are also fit better by elastic strain accumulation on a south-dipping fault plane along the southern border of the CSE basin rather than a vertical fault cross cutting it, which results in 9 mm/year of reverse slip and 6 mm/year of strike slip motion (Symithe & Calais, 2016). Seismicity has also been observed south of the CSE basin with a predominantly thrust component to the moment tensors, and a mean *P* axis consistent with the NNE-SSW compression orientation (Rodríguez et al., 2018). These observations are consistent with recent geological surveys that show the reverse faults, which border the CSE basin, affecting Quaternary alluvial sediments in the city of Port-au-Prince area

and to the east (Terrier et al., 2014). It seems therefore that while there may be evidence that the EPGF exists as a vertical structure across the CSE basin, present day motion is mainly accommodated along either one or a series of southward-dipping thrust faults along the southern border of the CSE basin.

## 2. Methods

### 2.1. Data

In April 2013, a temporary network of 27 broadband seismometers was deployed as part of the Trans-Haiti project (Figure 2). Most stations were deployed along a north-south transect across the island with a spacing of approximately 5–10 km. Continuous seismic data were recorded over a 16-month period at a sampling rate of 100 samples per second at all stations. Given the linearity of the network, E-W spatial coverage was improved by the addition of six permanent stations that were active at the same time as the temporary deployment (Figure 2 and supporting information Table S1). Data for these stations were downloaded from the Incorporated Research Institutions for Seismology (IRIS). Due to high anthropogenic noise levels at most stations, the highest signal-to-noise ratio was achieved using a four-pole Butterworth band-pass filter with corner frequencies at 1 and 6 Hz. This filter was applied to all stations prior to the manual picking of  $P$  and  $S$  phase arrivals. This created an initial data set of 1,055 local earthquakes that was used in this study.

### 2.2. 1-D Velocity Inversion

Previously derived velocity models for Haiti are limited to the immediate crustal region around the 2010 Haitian earthquake on the Southern Peninsula (Douilly et al., 2013; Douilly et al., 2016). However, there is likely to be strong lateral variation in seismic velocities between the tectonic domains as shown by the heterogeneous  $V_p/V_s$  ratios measured by receiver functions at the Tran-Haiti network stations (Corbeau, Rolandone, et al., 2017). We therefore derive new velocity models to account for these differences.

We use the VELEST code to invert  $P$  and  $S$  wave travel times for velocity models, station corrections, and hypocenter locations (Kissling et al., 1994). The method iteratively minimizes the root mean square (RMS) travel time residuals by changing velocities in layers that are specified by the user. We define the velocity layers to be optimal for the subsequent tomographic inversion of the data; velocities are therefore allowed to vary at  $-2, 0, 2, 4, 8, 12, 16, 20,$  and  $24$  km. An additional fixed velocity layer is added at  $40$  km for model stability; this depth is chosen based on the deepest Moho depth found by a receiver function study (Corbeau, Rolandone, et al., 2017). To ensure a stable inversion, we only use events with a minimum of five  $P$  phases, five  $S$  phases, and an azimuthal gap of less than  $240^\circ$ . This high-quality subset of the data consists of 201 earthquakes with 1,603  $P$  phase and 1,885  $S$  phase arrival times.

We evaluate three different starting 1-D velocity models for the inversion to test convergence and ensure our final model is not significantly biased by the starting parameters. These include models for southern Haiti (Douilly et al., 2013), Cuba (Moreno et al., 2002), and Jamaica (Wiggins-Grandison, 2004). The initial model for each inversion was interpolated from these models and extended to the Moho depth of  $40$  km using the ak-135 global model (Kennett et al., 1995). Initial inversions were used to test crustal structure and define a velocity model that best minimized RMS travel time residuals in the data. In these tests we did not invert for station corrections. In the final stage, we selected the best fitting velocity model and performed a final inversion, including station corrections, to produce the final 1-D model that best minimized RMS travel time residuals, termed a minimum 1-D model.

### 2.3. Earthquake Relocations

Using the minimum 1-D velocity model, hypocenter locations for the full catalog of 1,055 local earthquake were determined using the nonlinear NonLinLoc algorithm (Lomax et al., 2000). The algorithm computes a posterior density function (PDF) that represents a probability-derived solution to the inverse problem of earthquake location. The 1-D model is used to calculate travel times between all stations and nodes on a 3-D grid for the search region. Locations are then determined for each event using an Oct-Tree sampling algorithm, which successively searches over the PDF by subdividing cells increasingly finer until a termination criterion is reached. This generates complete earthquake location PDFs in 3-D space for the search volume.

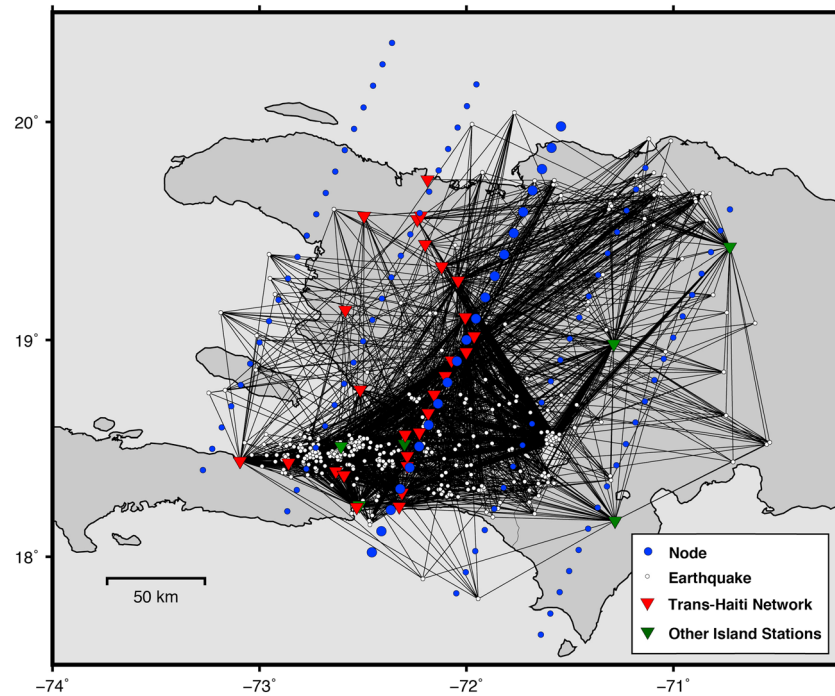


**Figure 2.** Station distribution and model parameterization of the SIMULPS tomographic inversion. Black lines are the event-receiver raypaths, and the central row of blue nodes corresponds to the final profile analyzed in this study. Inverted triangles represent the seismic stations. The other island stations refer to seismic stations from the Canadian Seismic Network, United States Geological Survey, Centro Nacional de Sismologia, and the Greater Antilles Seismic Program active at the same time as the Trans-Haiti Network.

#### 2.4. Magnitudes

Accurate magnitude determination is essential for assessing seismic hazard in any particular region. To determine local magnitudes ( $M_L$ ) for the earthquakes in our catalog, we use a new local magnitude scale based on the original definition by Richter (1935) and updated scale of Hutton and Boore (1987), which normalizes the scale at 17 km for an amplitude of 10 mm for a  $M_L$  3.0 earthquake.

$$\log(A) + 2 = -n \log\left(\frac{r}{17}\right) - K(r-17) + M_L - S \quad (1)$$

where  $A$  is equal to the measured amplitude,  $r$  is the hypocentral distance,  $S$  is an empirical station correction factor, while  $n$  and  $K$  are constants related to geometrical spreading and attenuation of seismic waves. In the new local magnitude scale, we derive,  $n = 0.90137$  and  $K = 0.0036789$  using the inversion procedure of Illsley-Kemp et al. (2017; Figure S1). For more information on how these constants were obtained, see Supporting Information S1.

In addition, seismic moments ( $M_o$ ) are estimated for each earthquake. There is no local  $M_L$ - $M_o$  scale determined for the region; therefore, we assumed a 1:1 conversion from  $M_L$  to  $M_b$  (body wave magnitude) and then used a global empirical relationship to convert  $M_b$  to  $M_o$  (Scordilis, 2006).

#### 2.5. Seismic Tomography

We used the SIMULPS code, which performs the tomographic inversion iteratively using a damped least-squares approach (Eberhart-Phillips, 1990; Thurber, 1983; Thurber & Eberhart-Phillips, 1999; Um & Thurber, 1987). The code jointly inverts for hypocentral locations and velocity models on up to a full 3-D grid, where  $V_p$  and  $V_p/V_s$  values are calculated at each grid node and linearly interpolated between nodes.

For the starting  $V_p$  model, we use the minimum 1-D model determined in this study. For the starting  $V_p/V_s$  model, we choose to use a constant value of 1.77, calculated using the gradient of the best-fit line through a

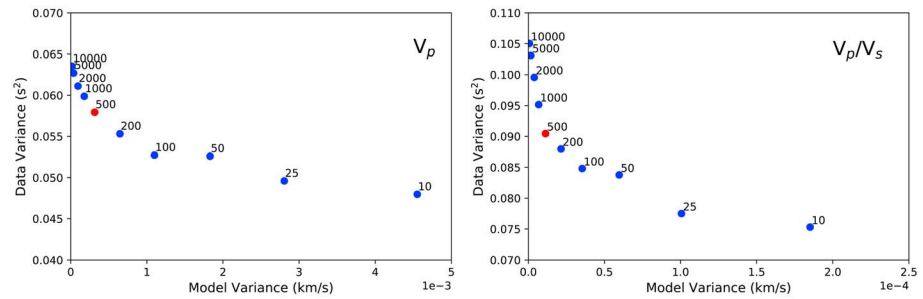


**Figure 3.** Trade-off curves for the reduction of data variance versus increase in model variance. Blue circles represent the values after one iteration of the inversion for different damping values, ranging from 10 to 10,000. The red circles represent the optimum damping values for both the  $V_p$  and  $V_p/V_s$  models, which were used in the final inversion.

Wadati diagram. In this way, we avoid as much bias in the starting model as possible. Events were selected from the NonLinLoc catalog located using the minimum 1-D model. To maximize the spatial coverage of the inversion, additional events were included compared to the 1-D inversion, extending the maximum azimuthal gap to  $270^\circ$ . In total, 437 events with robust location were selected, meaning they had a mean RMS travel time residual of less than 1 s and a minimum of six phases picked at more than five stations. The final inversion consisted of 4,843 manually picked seismic phases (2,619  $P$  phases and 2,224  $S$  phases) at 30 seismic stations.

In SIMULPS model, parameterization should be in part defined by the average station spacing and distribution. Our linear station distribution is not ideal for a full 3-D tomographic inversion. We therefore optimize our inversion procedure to assess the lateral variation in seismic velocities along the NNE-SSW profile, which is approximately perpendicular to the major tectonic domains and faults that form Hispaniola. We parameterize the model with a N-S horizontal node spacing of 12 km and a vertical node spacing of 4 km (Figure 2). For increased stability and to remove any off-structure influences on the final 2-D profile, additional nodes were added to the east and west at a spacing of 50 km to the main profile (Figure 2). We therefore refer to this a 2.5-D inversion from this point onward. In total, the main profile of the model consisted of 273  $V_p$  and 273  $V_p/V_s$  nodes along with 60 parameters pertaining to station corrections.

To prevent overfitting of the data, damping values were selected using a trade-off curve between data variance and model variance after a single iteration. For the final model, a value of 500 for both  $V_p$  and  $V_p/V_s$  models showed a good compromise between data misfit and model complexity (Figure 3).

The SIMULPS code offers several quantitative methods by which to assess spatial resolution within the model space. These include the derivative weight sum, which is a measure of ray density at each node, and the resolution diagonal element (RDE), which measures the dependency of the solution on individual model parameters. In addition, we also performed checkerboard resolution tests to assess the reliability and spatial resolution of the data. Checkerboard tests were performed by perturbing the model with  $\pm 10\%$   $V_p$  and  $V_p/V_s$  anomalies. This model was then used to generate synthetic travel times for each event-receiver pair. Random noise was then added to the arrival times with standard deviation of 0.2 s. The velocity model was then forgotten, and the synthetic data inverted to recover the anomalies using the same parameters as the final model.

### 3. Results

#### 3.1. 1-D Velocity Model

The three starting velocity models from southern Haiti (Douilly et al., 2013), Cuba (Moreno et al., 2002), and Jamaica (Wiggins-Grandison, 2004) had a mean RMS travel time residual of 0.74, 1.30, and 0.96 s, respectively, which reduced to 0.41, 0.40, and 0.43 s after the first inversion without station residuals. All models showed good convergence (Figure 4a); however, local minima in the RMS solution space were likely responsible for all models not reaching a single global minimum. As expected, the starting model from southern Haiti resulted in the best fitting velocity model for the data, with the best distribution of RMS travel time residuals (Figure 4c). The output of this model was therefore used as the starting model for the final inversion,

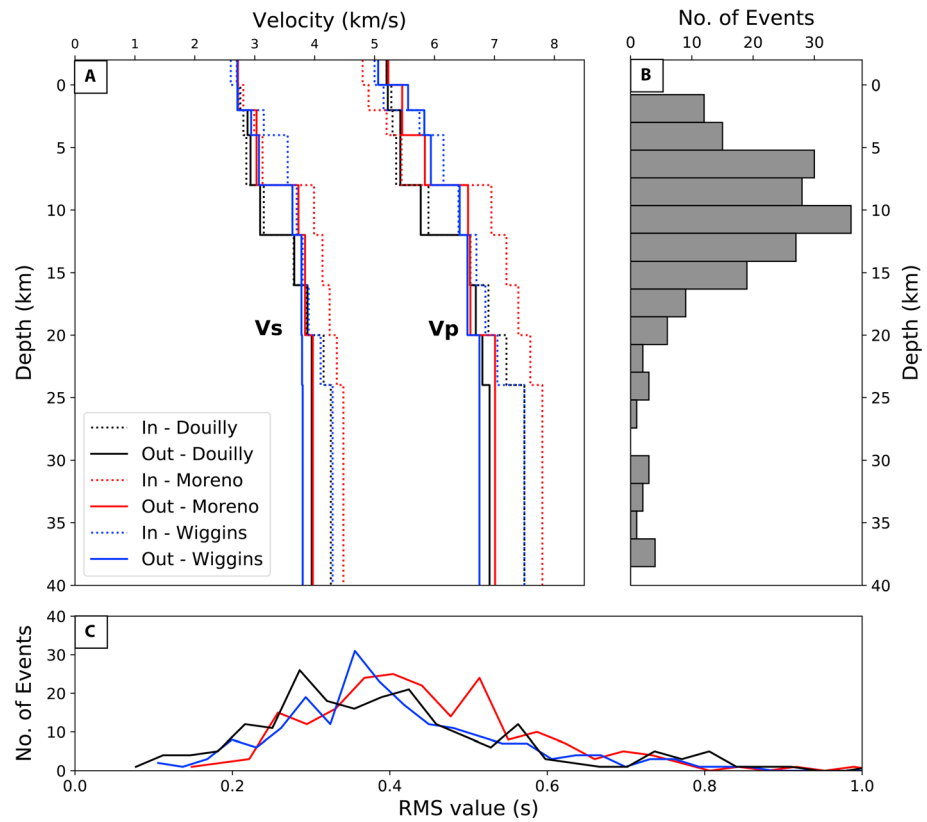


**Figure 4.** Results from the VELEST 1-D inversion without station corrections. (a) Velocity models for the three starting models from southern Haiti (Douilly et al., 2013), Cuba (Moreno et al., 2002), and Jamaica (Wiggins-Grandison, 2004). Dotted lines represent the input models and solid lines the output models. (b) Depth distribution of seismicity used in the inversion. (c) Distribution of root mean square (RMS) travel time residuals for the three output models.

including station corrections, to produce the minimum 1-D model (Figure 5 and Table 1). The minimum 1-D model, with station corrections (Table S1), had a final mean RMS of 0.33 s, again an improvement on the previous model in the inversion procedure.

### 3.2. Tomography

#### 3.2.1. Resolution

Resolution estimates using the checkerboard approach showed good recovery of velocity perturbations with a cell size of  $30 \times 10$  km within the central and southern regions of the model (Figure 6). There is good resolution to depths of 30 km in the  $V_p$  model and to 25 km in the  $V_p/V_s$  model. Amplitude recovery for the input anomalies is good within the well-resolved region; from the 10% input anomalies, the maximum recovered anomalies are 10% and 6% for the  $V_p$  and  $V_p/V_s$  models, respectively. To the north of the well-resolved region, there is smearing of velocity anomalies, due in part to the linearity of the seismic network and lack of crossing raypaths in the northern region of the model space.

The well-resolved region of the checkerboard model also coincides with the 0.1 RDE contour. We therefore choose a RDE value of 0.1 to approximate the maximum extent of resolution in the final models. The  $15 \times 7$  km checkerboard cell test demonstrates the ability to recover smaller anomalies in the central and southern region of the model (Figure 7). However, smearing of velocity anomalies is still prevalent in the northern part of the model space. In addition, the amplitude recovery of anomalies is reduced with maximum anomalies recovered being 6% for the  $V_p$  model and 4% for the  $V_p/V_s$  model.

#### 3.2.2. Model Performance

The final velocity model showed a decrease in RMS from 0.29 to 0.20 s over 10 iterations of the inversion. This represents a reduction in the model misfit by 31% over the starting model. Figure 8 shows cross

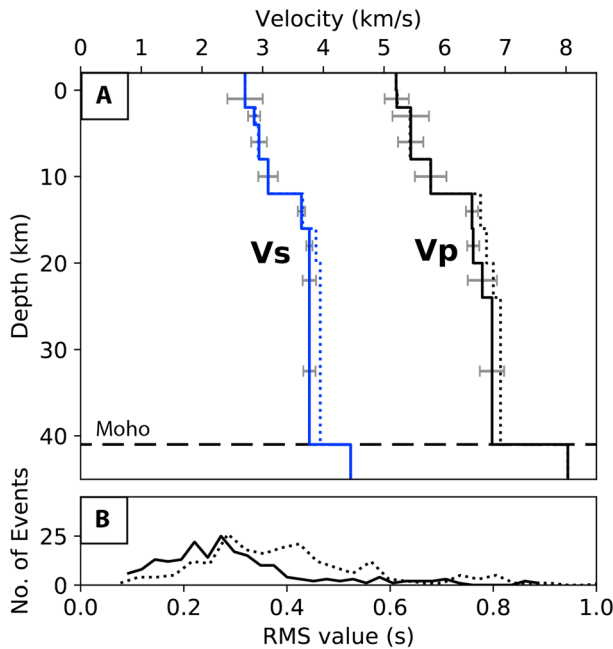


**Figure 5.** Results from the final VELEST 1-D inversion, including station corrections. (a) Velocity models for the starting model (dashed lines) and final minimum model (solid lines). Horizontal gray lines are the error bars. (b) Distribution of the root mean square (RMS) travel time residuals for the input (dashed line) and output model (solid line).

crust at depths of 10–20 km, high  $V_p/V_s$  values of 1.80–1.85 are observed beneath southern Haiti. This feature corresponds to the low-velocity anomaly observed in the  $V_p$  model. Further north in the model space, we observe a transition to lower  $V_p/V_s$  values of 1.70–1.75 at depths of 10–15 km beneath the Plateau Central basin.

### 3.3. Seismicity

#### 3.3.1. Catalog Completeness

The magnitude completeness ( $M_c$ ) for the catalog was estimated using the maximum-curvature method (Wiemer & Wyss, 2000), the magnitude bin with the greatest number of earthquakes (Figure 10). This returned a  $M_c$  value of 2.2 for the entire catalog, which was corrected to 2.4 since Woessner and Wiemer (2005) indicated that this method underestimates  $M_c$  by 0.1–0.2. Using this catalog completeness, a  $b$  value of  $1.07 \pm 0.09$  was calculated using the maximum-likelihood method (Aki, 1965).

#### 3.3.2. Hypocenter Locations

Nine hundred eighty-three earthquakes from the initial catalog of 1,055 yielded hypocenter locations with a mean RMS travel time residual less than 1 s (Figure 11). Absolute location errors for individual events were highly dependent on the relative location of the event to the network. In southern Haiti, where the spatial distribution of stations was good, location errors were typically in the order of  $\pm 1.2$  km horizontally and  $\pm 2.0$  km vertically. To the north, where station distribution was more linear, mean location errors increase to  $\pm 1.6$  km horizontally and  $\pm 4.0$  km vertically.

sections through the final  $V_p$  and  $V_p/V_s$  models along the primary profile, which corresponds to the central line of nodes in the inversion (Figure 2). As shown in the resolution test, the 0.1 RDE contour marks the outer limit of the well-resolved model space, which extends beneath the land surface of Haiti (–80 to 80 km in the model space) and to depths of 25 km beneath southern Haiti.

#### 3.2.3. $V_p$ Model

Multiple low-velocity anomalies, with a 5–8% decrease in  $V_p$  compared to the starting model, are present in the top 5 km of the crust along the profile (Figures 8 and 9). These anomalies correspond to the major sedimentary basins (CSE, Artibonite, and Plateau Central basins), which are identified by the regions of low-lying topography along the profile. Between these basins, mountainous regions such as the Massif de la Selle and Montagnes Noires have higher  $V_p$  values. Deeper in the crust, at depths of 5–25 km,  $V_p$  is still laterally heterogeneous. High  $V_p$  values are generally present beneath the Massif de la Selle and CSE basin. However, a low-velocity zone, with a 3–5% decrease in  $V_p$ , can be seen extending from the southern border of the CSE basin to a depth of 15 km. Equally, to the north of the CSE basin, another large low-velocity zone, with a 5–7% decrease in  $V_p$ , is present to a depth of 20 km.

#### 3.2.4. $V_p/V_s$ Model

High  $V_p/V_s$  values of  $>1.80$  are recovered for the upper 10 km of the crust for most of the resolved region of the model in the southern half of the model space (Figure 9). The largest anomaly is observed at the southern boundary of the CSE basin, with  $V_p/V_s$  values of 1.85–1.90. In the lower

crust at depths of 10–20 km, high  $V_p/V_s$  values of 1.80–1.85 are observed beneath southern Haiti. This feature corresponds to the low-velocity anomaly observed in the  $V_p$  model. Further north in the model space, we observe a transition to lower  $V_p/V_s$  values of 1.70–1.75 at depths of 10–15 km beneath the Plateau Central basin.

Earthquake locations were distributed across Haiti; however, significantly higher rates of seismicity were seen in the south compared with either the central or northern regions of the island. Two major clusters of seismicity were observed: the first around the epicenter of the 2010 Haitian earthquake, near to the city of Léogâne at  $\sim 72.5^\circ\text{W}$  along Haiti’s Southern Peninsula (Figure 12); the second was located at  $\sim 71.5^\circ\text{W}$  along the

**Table 1**  
Minimum 1-D Velocity Model From VELEST

Layer (km)	P wave velocity (km/s)	S wave velocity (km/s)
0	$5.21 \pm 0.20$	$2.71 \pm 0.29$
2	$5.44 \pm 0.30$	$2.86 \pm 0.10$
4	$5.44 \pm 0.21$	$2.94 \pm 0.13$
8	$5.77 \pm 0.26$	$3.09 \pm 0.16$
12	$6.45 \pm 0.09$	$3.64 \pm 0.06$
16	$6.47 \pm 0.10$	$3.75 \pm 0.04$
20	$6.62 \pm 0.24$	$3.77 \pm 0.11$
24	$6.78 \pm 0.20$	$3.77 \pm 0.09$
40	8.03	4.45



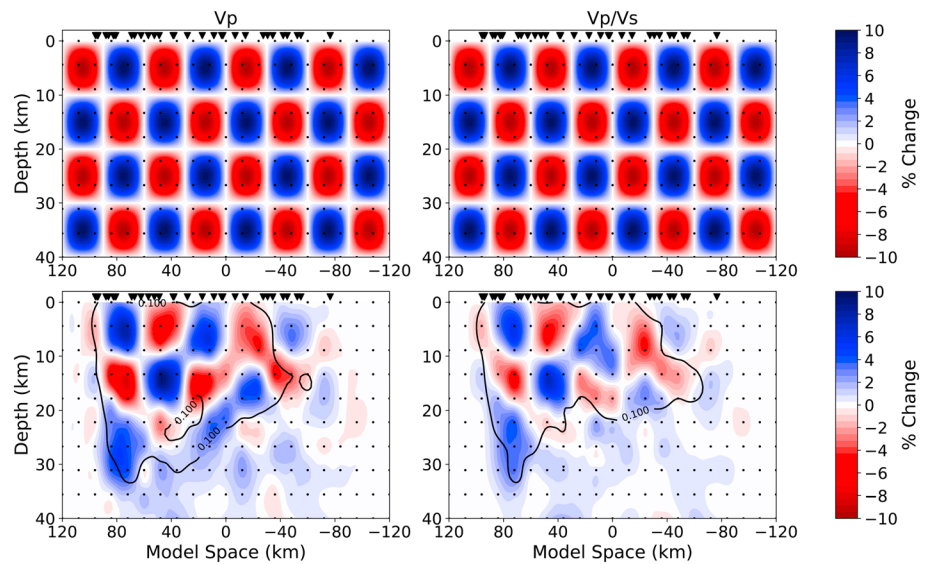


**Figure 6.** Checkerboard model test using a cell size of  $30 \times 10$  km. Top row shows the input velocity perturbation of alternating  $\pm 10\%$  velocity anomalies. Bottom row shows the recovered velocity anomalies. Black triangles show station locations within the model space. Black line in the output models shows the 0.1 contour of the resolution diagonal element matrix.

northern boundary of the CSE basin (Dominican Republic; Figure 13). In addition, sparse seismicity was seen throughout the Trans-Haiti deformation belt and along the SOFZ to the north.

Temporally, only one cluster of seismic activity was observed to clearly start and stop during our observation window. The cluster of seismic activity on the northern border of the CSE basin consisted of 121 earthquakes, 101 of which occurred during June and July 2013 (Figure 13). The remaining observed seismicity occurred at a consistent rate, including events around the epicenter of the 2010 earthquake, which were detected at a rate of 1–2 events per day (Figure 13).

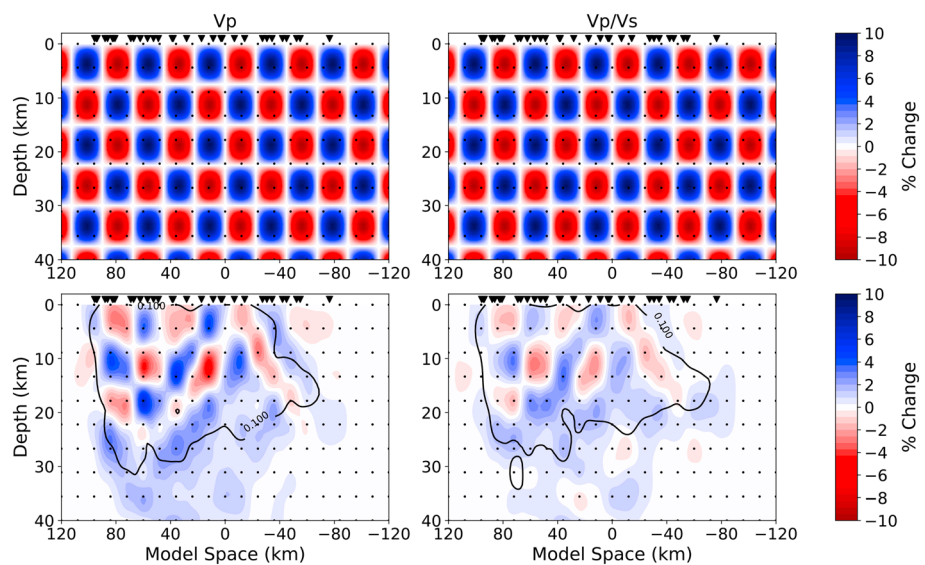


**Figure 7.** Checkerboard model test using a cell size  $15 \times 7$  km. Top row shows the input velocity perturbation of alternating  $\pm 10\%$  velocity anomalies. Bottom row shows the recovered velocity anomalies. Black triangles show station locations within the model space. Black line in output models shows the 0.1 contour of the resolution diagonal element matrix.

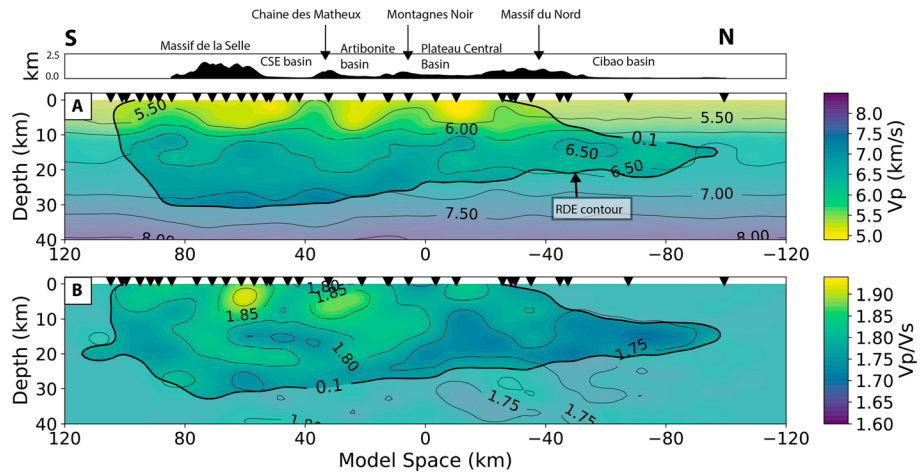


**Figure 8.** Final velocity models for a 2-D profile perpendicular to Haiti's major faults and tectonic terranes. Exact location of profile can be seen in Figure 2. Top box shows the topography along the profile with major geological features labeled. Black triangles represent the position of seismic stations within the model space. Bold black line indicates the 0.1 contour of the RDE matrix, model space outside this contour is considered unresolved and is therefore shaded. CSE = Cul-de-Sac-Enriquillo; RDE = resolution diagonal element.

Seismically active fault structures along Haiti's Southern Peninsula are shown by the projection of hypocenters onto cross sections (Figure 12). The orientation of the cross sections was chosen to be perpendicular to the seismically active structures that we observe in this study. Seismicity was observed at depths of 10–20 km south of the surface trace of the EPGF (Figure 12, profile AA'). Hypocenters also delineate a north-dipping structure between the depths of 5 and 20 km, with a strike of 255° and a dip of 70°N (Figure 12, profile CC'). Hypocenters in Figure 12, profile BB', only weakly delineate active structures. Further west, only diffuse seismicity was observed across the fault zone with hypocenters failing to delineate any clear structure (Figure 12, profile DD').

To the east, in southern Haiti and the Dominican Republic, the dominant strike of major faults is approximately NW-SE so cross sections were plotted perpendicular to this orientation (Figure 13). Beneath the

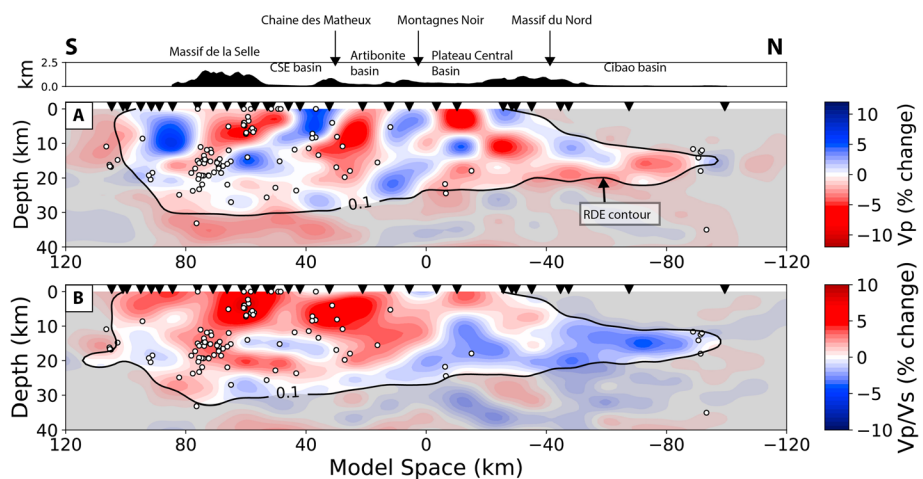


**Figure 9.** Final velocity models for a 2-D profile perpendicular to Haiti's major faults and tectonic terranes. Velocities are expressed as a percentage change from the input 1-D model as shown in Figure 5. Exact location of profile can be seen in Figure 2. Top box shows the topography along the profile with major geological features labeled. Black triangles represent the seismic stations within the model space. White circles are hypocenter locations within the model space for events located within 30 km of the profile. Bold black line indicated the 0.1 contour of the RDE matrix, model space outside this contour is considered unresolved and is therefore shaded. CSE = Cul-de-Sac-Enriquillo; RDE = resolution diagonal element.

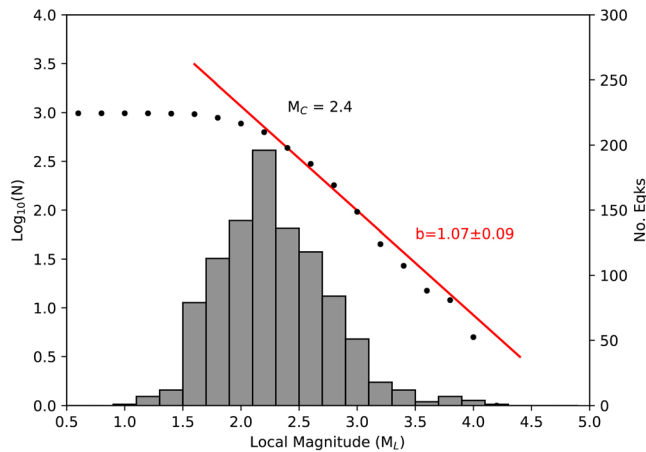


**Figure 10.** Magnitude distribution and  $b$  value analysis for earthquakes recorded by the Trans-Haiti network. Black dots (left axis) represent Gutenberg-Richter distribution in which  $\log_{10}(N)$  represents the number of earthquakes at a magnitude of  $M_L$  or greater. Gray bars (right axis) represent the number of earthquakes for each magnitude bin. Red line represents the ideal Gutenberg-Richter distribution for the  $b$  value of 1.07 calculated using the maximum likelihood method (Aki, 1965) with a magnitude completeness ( $M_C$ ) value of 2.4.

Massif de la Selle, seismicity weakly delineates a southward-dipping structure (Figure 13, profile AA'), that if projected to the surface would intersect at the southern boundary of the CSE basin. At the northern edge of the CSE basin, the cluster of seismicity observed was dominantly restricted to the upper 10 km of the crust; however, seismicity was present throughout the crust to 40 km (Figure 13, profile BB'). Hypocenter locations do not delineate any obvious linear structure near to the surface.

## 4. Discussion

### 4.1. Crustal $V_p$ and $V_p/V_s$ Structure

Body wave velocities can be used as a proxy to infer rock properties in the subsurface, varying according to composition, density, cracks, fluids, and temperature (Christensen, 1996; Shearer, 1988; Zhao et al., 1996). As shown in the tomographic models, Haiti has an extremely heterogeneous velocity structure (Figures 8 and 9), which is expected given the accretion of several tectonic terranes during the formation of the island. First-order variations relating to the compositional differences between the tectonic terranes are most obviously seen in the  $V_p/V_s$  structure across the island. The high  $V_p/V_s$  ratios of  $>1.80$  observed across southern and central Haiti can be linked to the dominantly mafic composition of the crust. For example, the southernmost part of Haiti is composed of the CLIP with a basaltic composition. However, in central Haiti, the high  $V_p/V_s$  ratios we observe are inconsistent with a crust of island arc origin and composition, as has been inferred in previous studies (Mann et al., 1991). High  $V_p/V_s$  ratios determined using receiver functions were also observed by Corbeau, Rolandone, et al. (2017), who suggested the possible inclusion of mafic material at a depth of 30–40 km in the crust. While our model cannot resolve features this deep, our high crustal  $V_p/V_s$  values to depths of 20 km indicate this mafic material may not be limited in extent to the base of the crust. This could suggest that Quaternary mafic volcanic facies, which are seen in limited outcrops at the surface

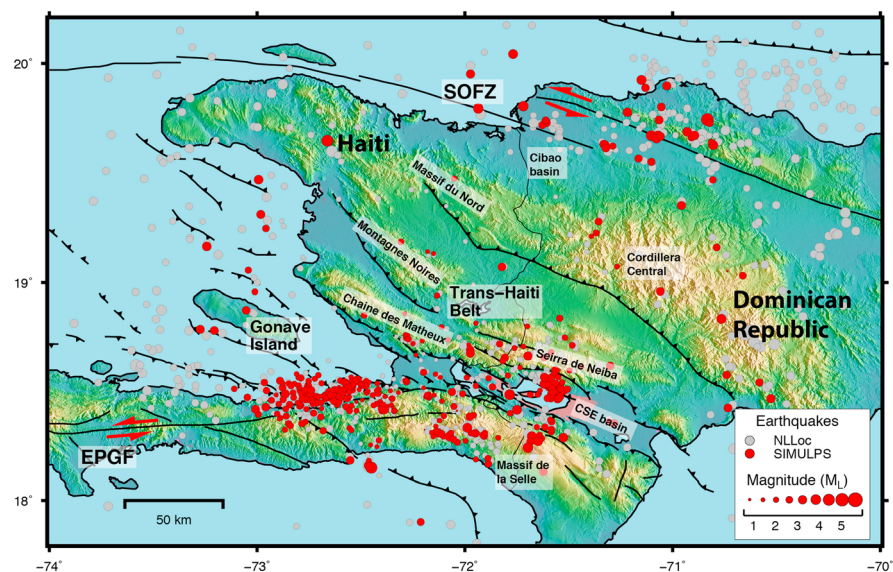


**Figure 11.** Seismicity recorded using the Trans-Haiti network for the 11-month period between June 2013 and April 2014. Red circles are epicenters for the 437 earthquakes determined during the joint inversion of hypocenters and velocities using SIMULPS. Gray circles are the epicenters of 983 earthquakes located using NonLinLoc and the best fit minimum 1-D velocity model from VELEST with station corrections. The size of each circle is scaled by the magnitude of each event. SOFZ = Septentrional-Oriente fault zone; CSE = Cul-de-Sac-Enriquillo; EPGF = Enriquillo-Plantain Garden Fault; NLLoc = NonLinLoc.

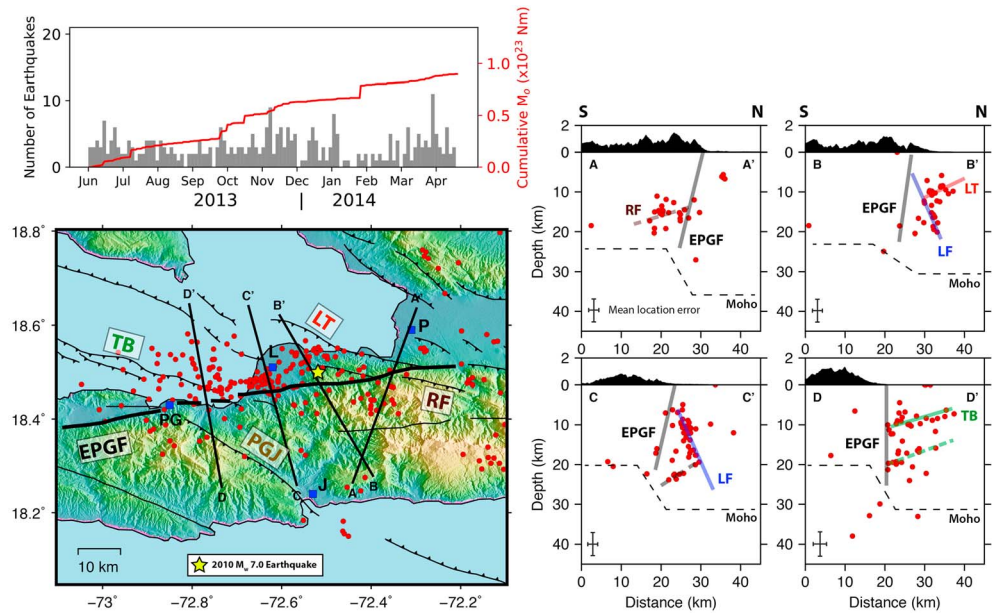


**Figure 12.** Seismicity observed on Haiti’s Southern Peninsula. Red circles are hypocenter locations from SIMULPS. Blue squares on the map represent cities; P = Port-au-Prince; L = Léogâne; PG = Petit Goâve; J = Jacmel. Labeled faults are EPGF = Enriquillo-Plantain Garden fault zone; LT = Lamentin fault; LE = Léogâne fault; TB = Trois Baies fault system; PGJ = Petit Goâve-Jacmel fault; RF = Redoute fault. The EPGF is assumed to be vertical to steeply south dipping based on its geomorphic expression (Prentice et al., 2010; Wessels et al., 2019). Moho depths are plotted using values from *P*-to-*S* receiver function for seismic stations in this region (Corbeau, Rolandone, et al., 2017). Top plot shows the temporal distribution of seismicity and cumulative seismic moment ( $M_0$ ) for seismicity along Haiti’s Southern Peninsula.

(Kamenov et al., 2011), are more common throughout the crust in central Haiti with the dense MgO rich material contributing to the elevated  $V_p/V_s$  ratios that we observe. However, sedimentary basins in the upper 5 km of the crust and pervasive faulting throughout the Trans-Haiti belt may also contribute to the high  $V_p/V_s$  ratios we observe.

The north of Haiti is by contrast characterized by lower  $V_p/V_s$  ratios of  $<1.75$ . The transition observed in our model between high and low  $V_p/V_s$  values occurs at the northern edge of the Plateau Central and San Juan

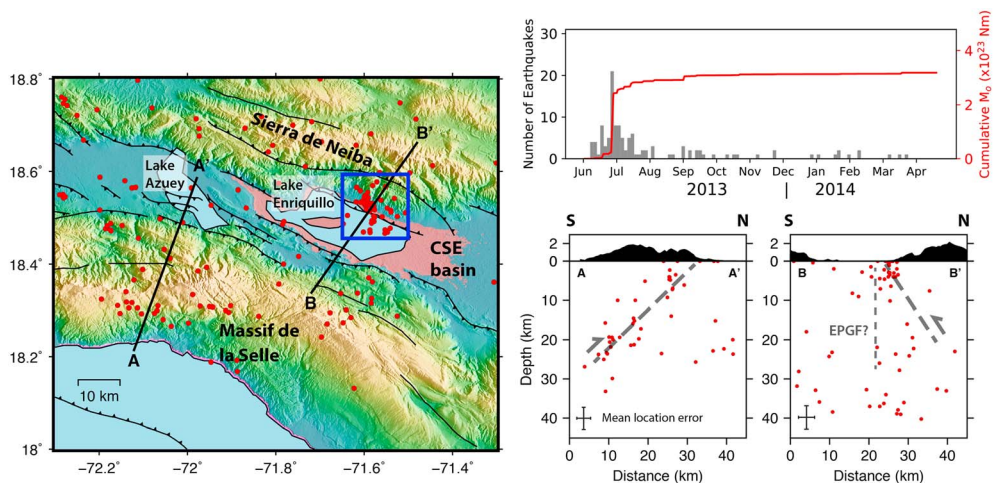


**Figure 13.** Seismicity observed around Lake Enriquillo in Haiti and the Dominican Republic. Red circles are hypocenter locations from SIMULPS. Top-right plot shows the temporal distribution of seismicity and cumulative seismic moment ( $M_0$ ) of the earthquake cluster north of Lake Enriquillo (blue box). CSE = Cul-de-Sac-Enriquillo; EPGF = Enriquillo-Plantain Garden Fault.

basins (Figure 9,  $-20$  km in the model space). This boundary likely parallels the Los Poloz-San Juan fault zone which bisects both Haiti and the Dominican Republic and has an approximate strike of  $130^\circ$ . This is consistent with the northern part of Haiti being composed of the Great Arc of the Caribbean island arc terrane, with a dominantly felsic composition giving the observed lower  $V_p/V_s$  ratios.

Elongate sedimentary basins such as the CSE, Plateau Central, and San Juan basins form the low-lying topography of the compressional Trans-Haiti belt, which extend to depths of 3–4 km in the crust (Mann & Lawrence, 1991). Our results show that these basins are characterized by low  $P$  wave velocities and high  $V_p/V_s$  ratios  $>1.85$ , which extend to depths of 8–10 km in our model (Figure 8). This would suggest that parts of these basins may be thicker than 3–4 km. However, it is also possible there may be an apparent thickening of the sedimentary basins due to the coarse vertical node spacing (4 km) used in the inversion procedure.

At depths of 10–12 km, the  $P$  wave velocity model is extremely heterogeneous throughout the profile (Figures 8 and 9). To the south beneath the Massif de la Selle,  $P$  wave velocities 6–8% faster than the starting 1-D model reflect the mafic composition of the CLIP terrane that forms the bulk composition of the crust south of the EPGF. However, a low-velocity zone with a 3–5% decrease in  $P$  wave velocities along, with increased  $V_p/V_s$  ratios of  $>1.80$ , is also imaged dipping south, which coincides with hypocenter locations (Figure 9). In previous studies, a southward-dipping structure thrust structure has been inferred from geodetic data (Symithe & Calais, 2016) and from seismicity (Rodriguez et al., 2018). Our observations are consistent with such a structure and are indicative of a significant deformation zone associated with this fault. The geometry of this fault is discussed in more detail in the next section. It is likely that fracturing within this deformation zone is causing the modified seismic velocities that we observe. Fluids may be present, but due to the resolution of our model, we do not observe the high  $V_p/V_s$  ratios, often  $>2.0$ , observed in some other tomographic studies of fault zone (Thurber et al., 1997).

The most obvious feature at midcrustal depths across central Haiti is a large low-velocity zone located to the north of the CSE basin and beneath the Chaines des Matheux (Figures 8 and 9, 30 km in the model space). There is no simple compositional reason for this anomaly based on geological models of the subsurface (Mann et al., 1991; Pubellier et al., 1991). Given the active deformation and observed seismicity on the southernmost faults of the Trans-Haiti belt in both this study and others, the decrease in velocities may relate to another extensive deformation zone and fracturing of the crust. The deformation may also relate to the suture zone between the CLIP to the south and the Great Arc to the North which is thought to be somewhere in the subsurface beneath the CSE basin. Increased  $V_p/V_s$  ratios ( $\sim 1.85$ ) in the same areas would suggest fluids are not pervasive among the fractures and faults; however, we are restricted by the same limitations of model resolution described above. The remainder of the Trans-Haiti belt, the northern region of the well-resolved model space, is characterized at midcrustal depths by both moderate increases and decreases in  $P$  wave velocities that likely relate to the heterogeneous crustal composition of the accretionary island arc terrane that forms most of central and northern Haiti.

Lower crustal properties are poorly constrained in both the  $P$  wave velocity and  $V_p/V_s$  models with no evidence of the Moho, including beneath the Southern Peninsula where crustal thickness has been estimated to be as thin as 20 km (Corbeau, Rolandone, et al., 2017). Across central Haiti, although below the resolution limit of our model, generally slower  $P$  wave velocities are observed from 25–40 km, which is also evident in the minimum 1-D velocity model. The slower velocities in the deeper parts of our models are explained well by a thicker crust of 40 km for the Trans-Haiti deformation belt across central Haiti (Corbeau, Rolandone, et al., 2017).

#### 4.2. Seismicity

Seismicity along Haiti's Southern Peninsula shows continued activity along faults that ruptured during the  $M_w$  7.0, 2010 earthquake (Figure 12). A large proportion of the seismicity in the area delineates structure dipping north at  $75^\circ$  and striking  $255^\circ$ , which is active between the depths of 5 and 20 km (Figure 12, profiles BB' and CC'). This structure is the Léogâne fault, observed and modeled in aftershock studies as the fault on which slip initiated in the 2010 earthquake (Calais et al., 2010; Douilly et al., 2013; Symithe et al., 2013). In map view, a spatial separation of the clusters along the Léogâne fault may also indicate that the fault is segmented beneath the basin (Figure 12, profile BB' and CC'). Wang et al. (2018) suggest that the Léogâne fault

forms a conjugate pair with southward-dipping faults such as the Lamentin thrust, accommodating shortening across the region. Possible stress transfer between the faults during the 2010 earthquake (Saint Fleur et al., 2015) and the continued seismicity we observe on both faults is consistent with these fault systems being coupled.

Seismicity located just south of the EPGF surface trace is shown to cluster at a depth of approximately 15 km (Figure 12, profile AA'). One interpretation of this seismicity is that it represents activity at depth on the main strike-slip portion of the EPGF or small fractures in the surrounding damage zone associated with faulting. However, a second interpretation is that these earthquakes occurred at the intersection of a blind thrust fault with the EPGF. In a recent study Wessels et al. (2019) mapped a new south-dipping thrust fault, which they called the Redoute Fault (Figure 12). We propose that the seismicity we observe is occurring at the subsurface intersection of this fault with the EPGF, which is consistent with proposed fault geometries (Wessels et al., 2019). The orientation of this structure is likely similar to the Petit Goâve-Jacmel fault imaged to the west (Douilly et al., 2016) and a southward-dipping oblique slip fault beneath the Massif de la Selle to the east (Symithe & Calais, 2016). Seismicity rates on the Léogâne fault are also seen to increase at depths of 7–10 km, the depth at which the fault intersects the EPGF (Figure 12, profile BB' and CC'). Therefore, an intersection of faults on the southern side of the EPGF may also explain the observed seismicity over the narrow depth range of 15–20 km. This would also suggest that the EPGF is acting as a mechanical barrier to the propagation of active faults, observed through slip and the lack of surface rupture during the 2010 earthquake.

To the east, there are two main hypotheses for regional fault geometry. The first suggests the eastward extension of a near vertical strand of the EPGF fault across the CSE basin, bisecting both Lake Azuei and Lake Enriquillo, based on evidence of curvilinear surface folds and shallow seismic structures (Mann et al., 1995; Wang et al., 2018). The second proposes that motion is primarily accommodated on NW-SE striking thrust faults on both the north and south margin of the CSE basin (Rodriguez et al., 2018; Saint Fleur et al., 2015; Symithe & Calais, 2016).

Our observations of seismicity beneath the Massif de la Selle show that hypocenters weakly delineate a broad southward-dipping fault structure that dips at  $\sim 40^\circ \pm 10$  (Figure 13, profile AA'). When projected to the surface, the fault would intersect the surface along the southern border of the CSE basin. A south-dipping fault at this location is consistent with linear fault propagation folds and reverse faults that have been mapped along the southern edge of the basin (Mann et al., 1991; Saint Fleur et al., 2015). Symithe and Calais (2016) also showed that a  $45^\circ$  southward-dipping oblique-slip fault beneath southern Haiti was consistent with GPS observations of oblique slip, as oppose to a near vertical strike-slip fault across the CSE basin. Moment tensors for seismicity recorded south of the CSE basin also have a dominantly thrust component with an average NNE-SSW  $P$  axis orientation (Rodriguez et al., 2018), which is consistent with the strain directions calculated from GPS data (Calais et al., 2016).

Seismicity observed north of Lake Enriquillo, in the Dominican Republic (Figure 13), is relatively poorly constrained due to the location of these events in relation to the seismic network. Therefore, the seismicity we observe is diffuse, especially with depth, and does not image any single structure. The epicenters are well clustered along the northern edge of the CSE basin though. Pubellier et al. (2000) mapped these faults to be left-lateral reverse faults dipping north, controlling the formation of both the lake and the basin, suggesting they represent the southernmost extent of the Trans-Haiti deformation belt. However, sonar surveys looking at the northern edge of the basin in Lake Azuei indicated there was little evidence for present day deformation (Wang et al., 2018). Further west, moving along strike into the Gulf of Gonâve ( $300^\circ$ ), offshore seismic data do show active compressional tectonics with north dipping reverse faults and folding perturbing the most recent sediments (Corbeau, Rolandone, Leroy, Meyer, et al., 2016). Moment tensors determined for this cluster also have a significant thrust component, again with  $P$  axis that indicates a NNE-SSW compression orientation (Corbeau, Clouard, et al., 2017). We therefore suggest that the active seismicity we observe is linked to a north-dipping reverse fault structure, similar to those observed in the field and part of the Trans-Haiti deformation belt (Pubellier et al., 2000).

Our observations of active seismicity are therefore much more consistent with the hypothesis that east of the CSE basin ( $-72.3^\circ\text{W } 18.6^\circ\text{N}$ ) NW-SE-orientated thrust faults are dominant on either margin of the basin, as opposed to a vertical strike-slip structure cross cutting it. To the south, a seismically active southward-

dipping oblique fault accommodates much of the present-day motion in the region. On the northern margin, seismic activity on north-dipping thrust faults indicates the southern-most part of the Tran-Haiti deformation belt is likely still active.

#### 4.3. Plate Boundary Faulting

The broad Caribbean-North American plate boundary is spread across several fault zones, and near Hispaniola motion is primarily accommodated by the EPGF in the south and the SOFZ in the north. However, the lateral extent and simplicity of these two major fault zones is being challenged by our new data set as well as recent geological and geodetic results (Saint Fleur et al., 2015; Symithe & Calais, 2016). We observe very little seismicity associated with a near vertical strike-slip fault, such as the EPGF. Instead, seismicity is associated with thrust structures such as the Léogâne fault, Trois Baies fault system, Petit Goâve-Jacmel fault, and other NE-SW striking faults dipping to the south, which are also imaged by low-velocity zones. These observations suggest that the EPGF transitions from a primarily strike-slip fault in western Haiti, with a minor compressional element, to oblique thrust faulting along the southern edge of the CSE basin and into the Dominican Republic. This represents a distinct change in the faulting geometry along Haiti's Southern Peninsula and an important constraint for our understanding of seismic hazard along this plate boundary fault.

In addition to the seismicity we detect in southern and central Hispaniola, we also record a large number of events in the north of the Dominican Republic and offshore (Figure 11). While these events are far outside our network and have large location uncertainties, it seems clear that the two most seismically active faults in this region are the SOFZ and the North Hispaniola fault, which lies offshore to the north. Rodriguez et al. (2018) also observed similarly high levels of seismicity associated with these faults; however, while the North Hispaniola fault has been mapped offshore (Rodriguez-Zurrunero et al., 2019), there is still much work needed to fully characterize the structure of the SOFZ which bisects much of the northern Dominican Republic onshore. The present day seismicity highlights the seismic hazard potential of the northern edge of the Caribbean-North American plate boundary, which can also be seen by the  $>M_w 7.0$  historical earthquakes associated these faults (Prentice et al., 2010; ten Brink et al., 2011).

## 5. Conclusions

Seismicity recorded from the Trans-Haiti network showed significant continued activity along faults associated with the  $M_w 7.0$ , 2010 earthquake on Haiti's Southern Peninsula throughout the observed time period (2013–2014). Hypocenters also revealed several south-dipping faults beneath southern Haiti, most likely with a significant thrust component, consistent with observed and modeled surface deformation. A cluster of seismic activity along the northern edge of the CSE basin also suggests the southernmost faults of the Trans-Haiti belt may still be active. The hypocenters indicate seismic activity along the SOFZ in the north of Haiti; however, poor station coverage to the north within the Trans-Haiti network meant a high magnitude detection threshold for this region of our study. Future deployments are needed to fully quantify seismic activity along the SOFZ.

Models of  $V_p$  and  $V_p/V_s$  have provided an image of Haiti's regional crustal structure across a NNE profile that bisects major tectonic domains and known-fault structures. The results show that Haiti is composed of multiple compositionally distinct tectonic domains, welded together during the eastward movement of the Caribbean plate. Low  $V_p/V_s$  ratios in the northern Haiti are consistent with a crust composed of island arc and fore-arc accretionary prism facies from the Greater Antilles arc. Central and southern Haiti are characterized by high  $V_p/V_s$  ratios, which are pervasive in the upper 20 km of the crust that we image. This fits well with the view that southern Haiti is composed of mafic facies from the CLIP terrane. However, it also suggests that the island arc crust of central Haiti has been significantly modified through compressional tectonics and possibly Quaternary mafic volcanism causing the elevated  $V_p/V_s$  ratios throughout the crust.

We also find evidence in low-velocity zones and seismicity that the EPGF transitions from a near vertical strike-slip fault to a southward dipping oblique-slip thrust fault moving eastward along Haiti's Southern Peninsula. This fault echoes other known thrust faults such as the Petit Goâve-Jacmel fault further to the

west. The transition is likely gradual along the Southern Peninsula but the EPGF certainly extends no further as a vertical strike-slip fault beyond its intersection with CSE basin.

### Acknowledgments

The work contained in this paper contains work conducted during a PhD study undertaken as part of the Natural Environment Research Council (NERC) Centre for Doctoral Training (CDT) in Oil & Gas (grant NE/M00578X/1). It is 50% funded by Southampton University via their Graduate School of the National Oceanography Centre Southampton (GSNOCS) and 50% funded by NERC both of whose support is gratefully acknowledged. We thank Seismic Equipment Infrastructure in the UK (SEIS-UK) for the use of the instruments and their computing facilities. The facilities of SEIS-UK are supported by NERC under agreement R8/H10/64. C.A.R. and N.H. acknowledge funding from NERC (NE/M003507/1 and NE/K010654/1) and the European Research Council (GA 638665). S.L., F.R., and J.C. acknowledge full support from the Institut des Sciences de la Terre Paris (ISTeP) to the Trans-Haiti project. E.C. acknowledges support from the Interreg Caraïbes/FEDER program to the "PREST" project and from the "Institut Universitaire de France". F. I. K. is funded through NERC studentship NE/L002531/1, a grant to GSNOCS from Roy Franklin OBE and the ECLIPSE Programme, funded by the New Zealand Ministry of Business, Innovation and Employment. We thank the Unité Technique de Sismologie of the Bureau des Mines et de l'Energie and the URGeo of the Université d'Etat d'Haiti for their help in the field. We thank Kelly Guerrier, Sophia Ulysse, and Frantz Saint Preux for their active contribution in installing the seismic stations and collecting the data. We also thank Tom Hall for his involvement in the fieldwork and data processing. The catalog of earthquakes located and used in this study can be found in the supporting information. Data for the Trans-Haiti Network, Canadian National Seismograph Network, and U.S. Geological Survey stations can be downloaded from the Incorporated Research Institutions for Seismology (IRIS).

### References

- Aki, K. (1965). Maximum likelihood estimate of  $b$  in the formula  $\log N = a - bM$  and its confidence limits. *Bulletin of the Earthquake Research Institute*, 43, 237–239.
- Bakun, W. H., Flores, C. H., & ten Brink, U. S. (2012). Significant earthquakes on the Enriquillo fault system, Hispaniola, 1500–2010: Implications for seismic hazard. *Bulletin of the Seismological Society of America*, 102(1), 18–30. <https://doi.org/10.1785/0120110077>
- Bourgeois, B., Andreieff, P., Lasnier, J., Gonnard, R., Le Metour, J., & Rancon, J.-P. (1988). Synthèse géologique de la République d'Haiti. *Technical Rep., Bureau des Mines et de L'Energie. Haiti, Port-au-Prince.*
- Burke, K. (1988). Tectonic evolution of the Caribbean. *Annual Review of Earth and Planetary Sciences*, 16(1), 201–230. <https://doi.org/10.1146/annurev.ea.16.050188.001221>
- Byrne, D., Suarez, G., & Mccann, W. (1985). Muertos Trough subduction—Microplate tectonics in the northern Caribbean? *Nature*, 317(6036), 420–421. <https://doi.org/10.1038/317420a0>
- Calais, E., & Mercier de Lépinay, B. (1995). Strike-slip tectonic processes in the northern Caribbean between Cuba and Hispaniola (windward passage). *Marine Geophysical Researches*, 17(1), 63–95. <https://doi.org/10.1007/BF01268051>
- Calais, E., Freed, A., Mattioli, G., Amelung, F., Jónsson, S., Jansma, P., et al. (2010). Transpressional rupture of an unmapped fault during the 2010 Haiti earthquake. *Nature Geoscience*, 3(11), 794–799. <https://doi.org/10.1038/ngeo992>
- Calais, É., Symithe, S., Mercier de Lépinay, B., & Prépetit, C. (2016). Plate boundary segmentation in the northeastern Caribbean from geodetic measurements and Neogene geological observations. *Comptes Rendus Geoscience*, 348(1), 42–51. <https://doi.org/10.1016/j.crte.2015.10.007>
- Calmus, T. (1983). Contribution à l'étude géologique du massif de Macaya (sud-ouest d'Haiti, Grandes Antilles): sa place dans l'évolution de l'orogène Nord-Caraïbe.
- Christensen, N. I. (1996). Poisson's ratio and crustal seismology. *Journal of Geophysical Research*, 101(B2), 3139–3156. <https://doi.org/10.1029/95JB03446>
- Corbeau, J., Clouard, V., Rolandone, F., Leroy, S. D., & Mercier de Lépinay, B. (2017). Is the local seismicity in Haiti capable of imaging the Northern Caribbean Subduction? AGU Fall Meeting Abstracts, 2017.
- Corbeau, J., Rolandone, F., Leroy, S., Mercier de Lépinay, B., Meyer, B., Ellouz-Zimmermann, N., & Momplaisir, R. (2016). The northern Caribbean plate boundary in the Jamaica Passage: Structure and seismic stratigraphy. *Tectonophysics*, 675, 209–226. <https://doi.org/10.1016/j.tecto.2016.03.022>
- Corbeau, J., Rolandone, F., Leroy, S., Guerrier, K., Keir, D., Stuart, G., et al. (2017). Crustal structure of western Hispaniola (Haiti) from a teleseismic receiver function study. *Tectonophysics*, 709, 9–19. <https://doi.org/10.1016/j.tecto.2017.04.029>
- Corbeau, J., Rolandone, F., Leroy, S., Meyer, B., Mercier de Lépinay, B., Ellouz-Zimmermann, N., & Momplaisir, R. (2016). How transpressive is the northern Caribbean plate boundary? *Tectonics*, 35, 1032–1046. <https://doi.org/10.1002/2015TC003996>
- Cowgill, E., Bernardin, T. S., Oskin, M. E., Bowles, C., Yikilmaz, M. B., Kreylos, O., et al. (2012). Interactive terrain visualization enables virtual field work during rapid scientific response to the 2010 Haiti earthquake. *Geosphere*, 8(4), 787–804. <https://doi.org/10.1130/GES00687.1>
- Cruz-Orosa, I., Sàbat, F., Ramos, E., Rivero, L., & Vázquez-Taset, Y. M. (2012). Structural evolution of the La Trocha fault zone: Oblique collision and strike-slip basins in the Cuban Orogen. *Tectonics*, 31, TC5001. <https://doi.org/10.1029/2011TC003045>
- Douilly, R., Aochi, H., Calais, E., & Freed, A. (2015). Three-dimensional dynamic rupture simulations across interacting faults: The  $M_w$  7.0, 2010, Haiti earthquake. *Journal of Geophysical Research: Solid Earth*, 120, 1108–1128. <https://doi.org/10.1002/2014JB011595>
- Douilly, R., Ellsworth, W. L., Kissling, E., Freed, A. M., Deschamps, A., & Mercier de Lépinay, B. (2016). 3-D velocity structure in southern Haiti from local earthquake tomography. *Journal of Geophysical Research: Solid Earth*, 121, 8813–8832. <https://doi.org/10.1002/2016JB013123>
- Douilly, R., Haase, J. S., Ellsworth, W. L., Bouin, M. P., Calais, E., Symithe, S. J., et al. (2013). Crustal structure and fault geometry of the 2010 Haiti earthquake from temporary seismometer deployments. *Bulletin of the Seismological Society of America*, 103(4), 2305–2325. <https://doi.org/10.1785/0120120303>
- Duncan, R., & Hargraves, R. (1984). Plate tectonic evolution of the Caribbean region in the mantle reference frame. *Geological Society of America Memoirs*, 162, 81–94. <https://doi.org/10.1130/MEM162-p81>
- Eberhart-Phillips, D. (1990). Three-dimensional P and S velocity structure in the Coalinga region, California. *Journal of Geophysical Research*, 95(B10), 15,343–15,363. <https://doi.org/10.1029/JB095iB10p15343>
- Geldmacher, J., Hanan, B., Blichert-Toft, J., Harpp, K., Hoernle, K., Hauff, F., et al. (2003). Hafnium isotopic variations in volcanic rocks from the Caribbean Large Igneous Province and Galápagos hot spot tracks. *Geochemistry, Geophysics, Geosystems*, 4(7), 1062. <https://doi.org/10.1029/2002GC000477>
- Granja-Bruña, J., Carbó-Gorosabel, A., Estrada, P. L., Muñoz-Martín, A., ten Brink, U., Ballesteros, M. G., et al. (2014). Morphostructure at the junction between the Beata ridge and the Greater Antilles island arc (offshore Hispaniola southern slope). *Tectonophysics*, 618, 138–163. <https://doi.org/10.1016/j.tecto.2014.02.001>
- Hashimoto, M., Fukushima, Y., & Fukahata, Y. (2011). Fan-delta uplift and mountain subsidence during the Haiti 2010 earthquake. *Nature Geoscience*, 4(4), 255–259. <https://doi.org/10.1038/ngeo1115>
- Hastie, A. R., Mitchell, S. F., Treloar, P. J., Kerr, A. C., Neill, I., & Barfod, D. N. (2013). Geochemical components in a Cretaceous island arc: The Th/La-(Ce/Ce\*) Nd diagram and implications for subduction initiation in the inter-American region. *Lithos*, 162–163, 57–69. <https://doi.org/10.1016/j.lithos.2012.12.001>
- Hayes, G., Briggs, R., Sladen, A., Fielding, E., Prentice, C., Hudnut, K., et al. (2010). Complex rupture during the 12 January 2010 Haiti earthquake. *Nature Geoscience*, 3(11), 800–805. <https://doi.org/10.1038/ngeo977>
- Heubeck, C., Mann, P., Dolan, J., & Monechi, S. (1991). Diachronous uplift and recycling of sedimentary basins during Cenozoic tectonic transpression, northeastern Caribbean plate margin. *Sedimentary Geology*, 70(1), 1–32. [https://doi.org/10.1016/0037-0738\(91\)90063-J](https://doi.org/10.1016/0037-0738(91)90063-J)
- Hutton, L., & Boore, D. M. (1987). The ML scale in southern California. *Bulletin of the Seismological Society of America*, 77, 2074–2094.
- Illsley-Kemp, F., Keir, D., Bull, J. M., Ayele, A., Hammond, J. O., Kendall, J. M., et al. (2017). Local earthquake magnitude scale and b-value for the Danakil region of northern Afar. *Bulletin of the Seismological Society of America*, 107(2), 521–531. <https://doi.org/10.1785/0120150253>



- Kamenov, G. D., Perfit, M. R., Lewis, J. F., Goss, A. R., Arévalo, R. Jr., & Shuster, R. D. (2011). Ancient lithospheric source for Quaternary lavas in Hispaniola. *Nature Geoscience*, 4(8), 554–557. <https://doi.org/10.1038/ngeo1203>
- Kennett, B., Engdahl, E., & Buland, R. (1995). Constraints on seismic velocities in the Earth from traveltimes. *Geophysical Journal International*, 122(1), 108–124. <https://doi.org/10.1111/j.1365-246X.1995.tb03540.x>
- Kissling, E., Ellsworth, W., Eberhart-Phillips, D., & Kradolfer, U. (1994). Initial reference models in local earthquake tomography. *Journal of Geophysical Research*, 99(B10), 19,635–19,646. <https://doi.org/10.1029/93JB03138>
- Kocel, E., Stewart, R. R., Mann, P., & Chang, L. (2016). Near-surface geophysical investigation of the 2010 Haiti earthquake epicentral area: Léogâne, Haiti. *Interpretation*, 4(1), T49–T61. <https://doi.org/10.1190/INT-2015-0038.1>
- Ladd, J. W., Worzel, J. L., & Watkins, J. S. (1977). Multifold seismic reflection records from the northern Venezuela Basin and the north slope of the Muertos Trench. In *Island arcs, deep sea trenches and back-arc basins* (pp. 41–56). Washington, DC: American Geophysical Union. <https://doi.org/10.1029/ME001p0041>
- Leroy, S., Ellou-Zimmermann, N., Corbeau, J., Rolandone, F., Mercier de Lépinay, B., Meyer, B., et al. (2015). Segmentation and kinematics of the North America-Caribbean plate boundary offshore Hispaniola. *Terra Nova*, 27(6), 467–478. <https://doi.org/10.1111/ter.12181>
- Leroy, S., Mauffret, A., Patriat, P., & Mercier de Lépinay, B. (2000). An alternative interpretation of the Cayman trough evolution from a reidentification of magnetic anomalies. *Geophysical Journal International*, 141(3), 539–557. <https://doi.org/10.1046/j.1365-246X.2000.00059.x>
- Lomax, A., Virieux, J., Volant, P., & Berge-Thierry, C. (2000). Probabilistic earthquake location in 3D and layered models. In *Advances in Seismic Event Location* (pp. 101–134). Dordrecht, Netherlands: Springer. [https://doi.org/10.1007/978-94-015-9536-0\\_5](https://doi.org/10.1007/978-94-015-9536-0_5)
- Manaker, D. M., Calais, E., Freed, A. M., Ali, S., Przybylski, P., Mattioli, G., et al. (2008). Interseismic plate coupling and strain partitioning in the northeastern Caribbean. *Geophysical Journal International*, 174(3), 889–903. <https://doi.org/10.1111/j.1365-246X.2008.03819.x>
- Mann, P., Draper, G., & Lewis, J. F. (1991). An overview of the geologic and tectonic development of Hispaniola. *Geological Society of America Special Papers*, 262, 1–28. <https://doi.org/10.1130/SPE262-p1>
- Mann, P., & Lawrence, S. (1991). Petroleum potential of southern Hispaniola. *Journal of Petroleum Geology*, 14(2), 291–308. <https://doi.org/10.1111/j.1747-5457.1991.tb00313.x>
- Mann, P., Taylor, F., Edwards, R. L., & Ku, T.-L. (1995). Actively evolving microplate formation by oblique collision and sideways motion along strike-slip faults: An example from the northeastern Caribbean plate margin. *Tectonophysics*, 246(1-3), 1–69. [https://doi.org/10.1016/0040-1951\(94\)00268-E](https://doi.org/10.1016/0040-1951(94)00268-E)
- Mauffret, A., & Leroy, S. (1997). Seismic stratigraphy and structure of the Caribbean igneous province. *Tectonophysics*, 283(1-4), 61–104. [https://doi.org/10.1016/S0040-1951\(97\)00103-0](https://doi.org/10.1016/S0040-1951(97)00103-0)
- Mauffret, A., Leroy, S., d'Acremont, É., Maillard, A., Mercier de Lépinay, B., Dos Reis, A. T., et al. (2001). Une coupe de la province volcanique Caraïbe: premiers résultats de la campagne sismique Casis 2. *Comptes Rendus de l'Académie des Sciences - Series IIA - Earth and Planetary Science*, 333, 659–667.
- Mercier de Lépinay, B., Deschamps, A., Klingelhoefer, F., Mazabraud, Y., Delouis, B., Clouard, V., et al. (2011). The 2010 Haiti earthquake: A complex fault pattern constrained by seismologic and tectonic observations. *Geophysical Research Letters*, 38, L22305. <https://doi.org/10.1029/2011GL049799>
- Momplaisir, R. (1986). Contribution à l'Etude Géologique de la partie orientale du massif de la hotte (presqu'île de sud d'Haiti): Synthèse structurale des marges de la presqu'île à partir de données sismiques. (PhD thesis). University Pierre-et-Marie-Curie (Paris VI).
- Moreno, B., Grandison, M., & Atakan, K. (2002). Crustal velocity model along the southern Cuban margin: Implications for the tectonic regime at an active plate boundary. *Geophysical Journal International*, 151(2), 632–645. <https://doi.org/10.1046/j.1365-246X.2002.01810.x>
- Nettles, M., & Hjörleifsdóttir, V. (2010). Earthquake source parameters for the 2010 January Haiti main shock and aftershock sequence. *Geophysical Journal International*, 183(1), 375–380. <https://doi.org/10.1111/j.1365-246X.2010.04732.x>
- Pindell, J., Maresch, W. V., Martens, U., & Stanek, K. (2012). The Greater Antillean Arc: Early Cretaceous origin and proposed relationship to Central American subduction mélanges: Implications for models of Caribbean evolution. *International Geology Review*, 54(2), 131–143. <https://doi.org/10.1080/00206814.2010.510008>
- Pindell, J. L. (1990). *Geological evolution of the Caribbean region: A plate-tectonic perspective* (pp. 339–374). The Caribbean Region: Boulder, CO: Geological Society of America, the Geology of North America H.
- Prentice, C., Mann, P., Crone, A., Gold, R., Hudnut, K., Briggs, R., et al. (2010). Seismic hazard of the Enriquillo-Plantain Garden fault in Haiti inferred from palaeoseismology. *Nature Geoscience*, 3(11), 789–793. <https://doi.org/10.1038/ngeo991>
- Pubellier, M., Mauffret, A., Leroy, S., Vila, J. M., & Amilcar, H. (2000). Plate boundary readjustment in oblique convergence: Example of the Neogene of Hispaniola, Greater Antilles. *Tectonics*, 19(4), 630–648. <https://doi.org/10.1029/2000TC900007>
- Pubellier, M., Vila, J.-M., & Boisson, D. (1991). North Caribbean neotectonic events: The Trans-Haitian fault system. Tertiary record of an oblique transcurrent shear zone uplifted in Hispaniola. *Tectonophysics*, 194(3), 217–236. [https://doi.org/10.1016/0040-1951\(91\)90262-Q](https://doi.org/10.1016/0040-1951(91)90262-Q)
- Richter, C. F. (1935). An instrumental earthquake magnitude scale. *Bulletin of the Seismological Society of America*, 25, 1–32.
- Rios, J., Mchugh, C., Hornbach, M., Mann, P., Wright, V., & Gurung, D. (2013). Holocene activity of the Enriquillo-Plantain Garden Fault in Lake Enriquillo derived from seismic stratigraphy. AGU Fall Meeting Abstracts, 2013.
- Rodriguez, J., Havskov, J., Sørensen, M. B., & Santos, L. F. (2018). Seismotectonics of south-west Dominican Republic using recent data. *Journal of Seismology*, 22(4), 883–896. <https://doi.org/10.1007/s10950-018-9738-9>
- Rodriguez-Zurrunero, A., Granja-Bruña, J., Carbó-Gorosabel, A., Muñoz-Martin, A., Gorosabel-Araus, J. M., De La Peña, L. G., et al. (2019). Submarine morpho-structure and active processes along the North American-Caribbean plate boundary (Dominican Republic sector). *Marine Geology*, 407, 121–147. <https://doi.org/10.1016/j.margeo.2018.10.010>
- Saint Fleur, N., Feuillet, N., Grandin, R., Jacques, E., Weil-Accardo, J., & Klinger, Y. (2015). Seismotectonics of southern Haiti: A new faulting model for the 12 January 2010 M7.0 earthquake. *Geophysical Research Letters*, 42, 10,273–10,281. <https://doi.org/10.1002/2015GL065505>
- Scordilis, E. (2006). Empirical global relations converting M<sub>S</sub> and m<sub>b</sub> to moment magnitude. *Journal of Seismology*, 10(2), 225–236. <https://doi.org/10.1007/s10950-006-9012-4>
- Shearer, P. M. (1988). Cracked media, Poisson's ratio and the structure of the upper oceanic crust. *Geophysical Journal International*, 92(2), 357–362. <https://doi.org/10.1111/j.1365-246X.1988.tb01149.x>
- Symithe, S., & Calais, E. (2016). Present-day shortening in Southern Haiti from GPS measurements and implications for seismic hazard. *Tectonophysics*, 679, 117–124. <https://doi.org/10.1016/j.tecto.2016.04.034>

- Symithe, S. J., Calais, E., Haase, J. S., Freed, A. M., & Douilly, R. (2013). Coseismic slip distribution of the 2010 M 7.0 Haiti earthquake and resulting stress changes on regional faults. *Bulletin of the Seismological Society of America*, 103(4), 2326–2343. <https://doi.org/10.1785/0120120306>
- ten Brink, U. S., Bakun, W. H., & Flores, C. H. (2011). Historical perspective on seismic hazard to Hispaniola and the northeast Caribbean region. *Journal of Geophysical Research*, 116, B12318. <https://doi.org/10.1029/2011JB008497>
- Terrier, M., Bialkowski, A., Nachbaur, A., Pr  petit, C., & Joseph, Y. (2014). Revision of the geological context of the Port-au-Prince metropolitan area, Haiti: Implications for slope failures and seismic hazard assessment. *Natural Hazards and Earth System Sciences*, 14(9), 2577–2587. <https://doi.org/10.5194/nhess-14-2577-2014>
- Thurber, C., & Eberhart-Phillips, D. (1999). Local earthquake tomography with flexible gridding. *Computers & Geosciences*, 25(7), 809–818. [https://doi.org/10.1016/S0098-3004\(99\)00007-2](https://doi.org/10.1016/S0098-3004(99)00007-2)
- Thurber, C., Roecker, S., Ellsworth, W., Chen, Y., Lutter, W., & Sessions, R. (1997). Two-dimensional seismic image of the San Andreas Fault in the Northern Gabilan range, Central California: Evidence for fluids in the fault zone. *Geophysical Research Letters*, 24(13), 1591–1594. <https://doi.org/10.1029/97GL01435>
- Thurber, C. H. (1983). Earthquake locations and three-dimensional crustal structure in the Coyote Lake area, central California. *Journal of Geophysical Research*, 88(B10), 8226–8236. <https://doi.org/10.1029/JB088iB10p08226>
- Um, J., & Thurber, C. (1987). A fast algorithm for two-point seismic ray tracing. *Bulletin of the Seismological Society of America*, 77, 972–986. <https://doi.org/10.1007/s11589-005-0062-4>
- Wang, J., Mann, P., & Stewart, R. R. (2018). Late Holocene structural style and seismicity of highly transpressional faults in southern Haiti. *Tectonics*, 37(10), 3834–3852. <https://doi.org/10.1029/2017TC004920>
- Wessels, R. J., Ellouz-Zimmermann, N., Bellahsen, N., Hamon, Y., Rosenberg, C., Deschamps, R., et al. (2019). Polyphase tectonic history of the Southern Peninsula, Haiti: From folding-and-thrusting to transpressive strike-slip. *Tectonophysics*, 751, 125–149. <https://doi.org/10.1016/j.tecto.2018.12.011>
- Wiemer, S., & Wyss, M. (2000). Minimum magnitude of completeness in earthquake catalogs: Examples from Alaska, the western United States, and Japan. *Bulletin of the Seismological Society of America*, 90(4), 859–869. <https://doi.org/10.1785/0119990114>
- Wiggins-Grandison, M. D. (2004). Simultaneous inversion for local earthquake hypocentres, station corrections and 1-D velocity model of the Jamaican crust. *Earth and Planetary Science Letters*, 224(1-2), 229–240. <https://doi.org/10.1016/j.epsl.2004.05.009>
- Woessner, J., & Wiemer, S. (2005). Assessing the quality of earthquake catalogues: Estimating the magnitude of completeness and its uncertainty. *Bulletin of the Seismological Society of America*, 95(2), 684–698. <https://doi.org/10.1785/0120040007>
- Zhao, D., Kanamori, H., Negishi, H., & Wiens, D. (1996). Tomography of the source area of the 1995 Kobe earthquake: Evidence for fluids at the hypocenter? *Science*, 274(5294), 1891–1894. <https://doi.org/10.1126/science.274.5294.1891>